Equal-Spin Andreev Reflection in Junctions of Spin-Resolved Quantum Hall Bulk State and Spin-Singlet Superconductor

Sadashige Matsuo,[1,*] Kento Ueda,[1] Shoji Baba,[1] Hiroshi Kamata,[1,2] Mizuki Tateno,[1] Javad Shabani,[3] Christopher J. Palmstrøm,[3] and Seigo Tarucha[1,2]

[1] *Department of Applied Physics, University of Tokyo, 7-3-1 Hongo, Bunkyo-ku, Tokyo 113-8656, Japan*

[2] *RIKEN, Center for Emergent Matter Science, Hirosawa 2-1, Wako-shi, Saitama 351-0198, Japan*

[3] *California NanoSystems Institute, University of California, Santa Barbara, CA 93106, USA*

arXiv:1703.03189v1 [cond-mat.mes-hall] 9 Mar 2017

The recent development of superconducting spintronics has revealed the spin-triplet superconducting proximity effect from a spin-singlet superconductor into a spin-polarized normal metal. In addition recently superconducting junctions using semiconductors are in demand for highly controlled experiments to engineer topological superconductivity. Here we report experimental observation of Andreev reflection in junctions of spin-resolved quantum Hall (QH) states in an InAs quantum well and the spin-singlet superconductor NbTi. The measured conductance indicates a sub-gap feature and two peaks on the outer side of the sub-gap feature in the QH plateau-transition regime increases. The observed structures can be explained by considering transport with Andreev reflection from two channels, one originating from equal-spin Andreev reflection intermediated by spin-flip processes and second arising from normal Andreev reflection. This result indicates the possibility to induce the superconducting proximity gap in the the QH bulk state, and the possibility for the development of superconducting spintronics in semiconductor devices.

A junction of superconductor and normal metal is a platform to observe superconducting proximity effect, in which the superconducting property penetrates to the normal metal. In a microscopic description of the proximity effect, an electron in the normal metal enters the spin-singlet superconductor, forming a Cooper pair with another electron with opposite spin, reflecting a hole into the normal metal, in a process called Andreev reflection (AR) [1]. In this picture, no AR is expected in the case of a fully spin polarized normal metal, however recently, theoretical and experimental studies in junctions with spin-polarized normal metal, revealed existence of the spin-triplet superconducting proximity effect [2–8]. The spin-triplet proximity effect is only allowed when spin-flip processes intermediate "equal-spin" AR, which is possible due to the presence of magnetization inhomogeneity or spin-orbit interaction [9, 10]. Ferromagnetic metal has been utilized in experiments of superconducting spintronics to date. A semiconductor material however offers several advantages, including the control of carrier density and spin filling through electrical gating and magnetic field, and the possibility of ballistic transport in micron sized devices. Furthermore strong spin-orbit interaction can be utilized in two dimensional electron gases (2DEGs) in narrow gap semiconductors such as InAs and InSb [11–14]. These features favor the formation of spin-polarized states when the 2DEG is in the quantum Hall (QH) regime. Indeed, there are several experimental reports focusing on superconductor-semiconductor junctions in the QH regime [15–20]. However, all of these experiments have focused on the spin-degenerate QH states and the spin-triplet proximity effect has yet to be experimentally addressed, despite theoretical predictions of spin-triplet supercurrent in Josephson junctions with weak links of spin resolved QH edge channels [10]. Additionally, if the superconducting proximity gap is induced into the spin-resolved QH state, the system can be a topological superconductor [21] and give a new platform to realize the Majorana Fermions [22, 23] whose signatures have recently been reported [24–31].

Here we report an experimental study on electron transport in junctions between spin-resolved QH states and spin-singlet superconductors. We prepared junctions consisting of a high mobility InAs quantum well (QW) with NbTi contacts. The NbTi layers are contacted to the sides of the mesa containing the QW, minimizing the damage to the 2DEG. The 2DEG possesses a large g-factor, high mobility, and strong spin-orbit interaction, all necessary ingredients for coexistence of superconductivity and spin-resolved QH states. We observe spin-resolved quantized steps at magnetic fields below the superconducting critical field, 7 T, and find that the differential conductance has a dip or a peak structure as a sub-gap feature in all QH plateau-transition regimes of filling factor between 0 to 4. Additionally, we find two side peaks on the outer side of the sub-gap feature. We conclude that the structures observed here are a result of the equal-spin AR between the spin-resolved QH bulk states and the superconductor.

We fabricated junction devices from an InAs QW grown by molecular beam epitaxy [32, 33] with carrier density 3×10^{11} cm^{-2} and mobility 3×10^5 cm^{2}V^{-1}s^{-1}. (The material stack is represented in Supplemental Material (SM).) The cross section of the device is schematically represented in Fig. 1(a). Sputtered NbTi with the critical field of 7.0 T and the critical temperature of 6.5 K contacts the edge of the 2DEG and a top gate structure is fabricated using an insulating layer of cross-linked PMMA (see SM for details). The optical microscope photo in Fig. 1(b) shows the top view of the device. The two junctions are separated by 20 μm, so this device is assumed to have two independent junctions. We measured the two-terminal differential conductance in a He3He4 dilution refridgerator with a base temperature of 50 mK.

Figure 1(c) shows the measured dI/dV vs. $V_{\rm sd}$ at B =0 T. The dI/dV is enhanced in the range of -0.71 mV $< V_{\rm sd} < 0.71$ mV. This conductance enhancement arises from AR [1, 34] and only appears for the bias voltage in the junction less than the superconducting bulk gap energy Δ_{bulk}. Therefore, we evaluate the Δ_{bulk} as approximately 0.35 meV. The observation of the sub-gap feature guarantees that the junction has enough quality to study AR between the superconductor and spin-resolved QH state.

Figure 1(d) shows dI/dV vs. the top gate voltage, $V_{\rm tg}$. dI/dV gradually decreases with decreasing $V_{\rm tg}$ and becomes pinched off for $V_{\rm tg} <$ -1.38 V. This indicates that the top gating efficiently varies the 2DEG carrier density but not necessarily near the junction. We measured dI/dV vs. $V_{\rm sd}$ for various values of $V_{\rm tg}$ to examine the effect of top gating on the sub-gap conductance. We derived the differential resistance as given by $dV/dI = (dI/dV)^{-1}$ and then subtracted dV/dI measured at $V_{\rm sd} = 2.0$ mV to eliminate the normal state resistance including a series resistance due to the InAs QW away from the junction. The result is shown in Fig. 1(e) for three different values of $V_{\rm tg}$ =0, -0.45, and -0.625 V by the purple, blue, and green curve, respectively. It is clear to see that $dV/dI(V_{\rm sd}) - dV/dI(2.0$ mV) displays a pronounced reduction (or conductance enhancement) within the gap, and the reduction increases as $V_{\rm tg}$ is made more positive. If the top gating only varies the carrier density away from the junction, the dV/dI reduction below the gap should be constant with $V_{\rm tg}$. Therefore, the result of Fig. 1(e) indicates that the top gating is efficient enough to vary the carrier density in the InAs QW near the superconducting junction. In Fig. 1(e), $V_{\rm sd}$ to characterize the superconducting gap decreases as $V_{\rm tg}$ is made more positive. The $V_{\rm sd}$ shift is due to the change in the voltage dropped over the junctions when the series resistance of the 2DEG is altered. Schematics of the equivalent circuit for the device are shown in Fig. 1(f). In the constant voltage bias measurement, the effective junction voltage decreases as the carrier density of the QW decreases with decreasing $V_{\rm tg}$. Herein the applied voltage of $V_{\rm sd}$ is assumed to only

drop across the junctions in the saturation region. Therefore we evaluate $\Delta_{bulk} \simeq 0.35$ meV. This Δ_{bulk} is smaller than the value of 0.99 meV, predicted from the critical temperature with conventional BCS theory. A reduced Δ_{bulk} has been reported in previous studies [35], and assigned to the normal reflection in the junction as a possible origin. The normal reflection can lift the degeneracy of the gap, making the energy lower [36].

In Fig. 2(a), we present plots of measured dI/dV as a function of $V_{\rm tg}$ at out-of-plane magnetic field $B = 2.4$ and 4.0 T. The well-defined plateaus at integer multiples of e^2/h which originate from the QH edge transport are clearly seen. From this observation, it is confirmed that the applied fields are strong enough to resolve the spin degeneracy, but significantly smaller than the critical field of the NbTi, implying that the superconductivity and the spin-resolved QH states coexist.

dI/dV vs. $V_{\rm sd}$ measured in the range of $V_{\rm tg}$ between -1.5 V and 0 V is represented in Fig. 2(b), and (c) for $B = 2.4$ T, and 4.0 T, respectively. dI/dV traces measured for magnetic fields spanning the conductance range ne^2/h to $(n+1)e^2/h$ with $n = 0, 1, 2...$ are shown in the separate panels to highlight the sub-gap structure in the transition regions between plateaus. For example, dI/dV at $B = 2.4$ T between $0 < dI/dV < e^2/h$ is shown in the leftmost panel of Fig. 3(b).

In the transition regions between the conductance plateaus, we find pronounced sub-gap features appearing as a dip, a peak and then a dip at around $V_{\rm sd} = 0$ V from the lower to the upper plateau in all panels. Similar sub-gap features are previously reported for the junctions of two NbN superconductors and a spin-degenerated QH state in an InAs QW [15]. However, the underlying physics of the sub-gap feature remains to be elucidated. More interestingly in Fig. 2(b) and (c), the center peak appears broad in some traces and even split into two in others. In addition to a center dip or peak structure we observe a side peak. For example, it is clear to see two side peaks at $V_{\rm sd} = \pm 1.8$ mV in addition to a peak at $V_{\rm sd} = 0$ V for the curves at $dI/dV \simeq 2.5e^2/h$ in the right panel of Fig. 2(c).

The sub-gap conductance enhancement indicated by the observation of a zero-bias peak can be assigned to AR in the junction having a low potential barrier. In contrast, if the potential barrier is so large that normal reflection is more dominant than AR, a dip rather than a peak can appear according to the Blonder, Tinkham, and Klapwijk (BTK) theory [34]. Therefore we assign the peak (dip) structure observed in the plateau-transition regime to AR (normal reflection), and then the change of the sub-gap feature in Fig. 2 (b) and (c) can be simply explained by considering the change of the junction potential barrier depending on $V_{\rm tg}$. For the transport through the QH state it is well established that the dominant contribution arises from the QH bulk state in the plateau-transition regime and from the QH edge state in the plateau regime. Herein, we deduce that the sub-gap feature, especially the peak structure is originated from AR in the junction between the superconductor and the spin-resolved QH bulk state. A finite amount of equal-spin AR can be expected for a 2DEG with strong spin-orbit interaction according to recent theoretical studies [9, 10]. Therefore, we here assume coexistence of equal-spin AR and normal AR, corresponding to AR intermediated with and without a spin-flip process respectively, as schematically shown in Fig. 3(a).

In order to more quantitatively interpret the sub-gap features including the side peaks, we construct a model based on the BTK theory. In this theory, the normalized differential conductance of the junction, $G_{\rm int}(V_{\rm sd}, Z, T, \Delta)$, can be written as

$$G_{\rm int}(V_{\rm sd}, Z, T, \Delta) = \int_{-\infty}^{\infty} \frac{df(E - V_{\rm sd}, T)}{dV_{\rm sd}} (1 + A(E, Z, \Delta) - B(E, Z, \Delta)) dE, \quad (1)$$

where $f(E), T, \Delta$ and Z are the Fermi-Dirac distribution function, temperature, superconducting gap and the dimensionless parameter representing the potential barrier in the junction, respectively. $A(B)$ is the probability of the equal-spin AR (normal reflection) defined in the BTK theory [34]. However, this standard BTK theory cannot explain the coexistence of side peaks and sub-gap feature as observed in Fig. 2(b) and (c). Herein, to apply the BTK theory for such cases, we assume two different transport channels in the proximity region, labeled channel α in which the equal-spin AR occurs and channel β with no spin-flip process. A schematic representation of the transport in these channels is shown in Fig. 3(a). The channel α can generate the sub-gap features reflecting the conductance enhancement due to the equal-spin AR, while the channel β can generate the side peaks reflecting the quasiparticle peaks of the superconducting bulk gap energy via normal reflection. Then, the normalized differential conductance of the junction can be written as

$$P \times G^{\alpha}_{\rm int}(V_{\rm sd}, Z_{\alpha}, T, \Delta_{\alpha}) + (1 - P) \times G^{\beta}_{\rm int}(V_{\rm sd}, Z_{\beta}, T, \Delta_{\beta}), \quad (2)$$

where $G^{\alpha}_{\rm int}, G^{\beta}_{\rm int}, Z_{\alpha}, {\rm and} Z_{\beta}$ are the normalized differential conductance of the channel α, the normalized differential conductance of the channel β, the parameter Z in the eqn. (1) of the channel α and that of the channel β, respectively. Δ_{α}, and Δ_{β} are the proximity gap energy, and the bulk gap energy, respectively. Parameter P indicates the relative contribution of the two AR channels. We note that the appearance of two superconducting gaps are theoretically

discussed in the case of coexistence of spin-singlet and triplet superconducting pair amplitude [37, 38]. We executed numerical calculations to fit the experimental data (see SM).

The best fitting result is shown in Fig. 3(b) by the solid lines plotted alongside the experimental data at 4.0 T. The obtained Δ_α and Δ_β are plotted as a function of dI/dV in Fig. 3(c). dI/dV for the x-axis is the differential conductance of the normal state measured at $V_{\rm sd} = 3.5$ mV in units of e^2/h and indexed by g. Δ_β is derived from the side peak positions and has a convex upward trend in each plateau-transition regime between plateaus of g= 0 and 1, 1 and 2, and 2 and 3, respectively. These Δ_β values are larger than the true bulk gap due to the dissipation in the QH bulk state (the equivalent circuit is the same as shown in Fig. 1(f)). We assume that the superconducting bulk gap $\Delta_{bulk} = 0.35$ meV which is derived in Fig. 1(c) is unchanged with $V_{\rm tg}$ and therefore Δ_β in Fig. 3(c) should be equal to Δ_{bulk}. This assumption is probably valid because the observed Δ_β in the plateau regime where there is no dissipation is consistent with Δ_{bulk} (see SM). Then we use the same equivalent circuit model as used for evaluating Δ_{bulk} to calibrate the value of Δ_α and finally obtain the true proximity gap of $\Delta_{\rm triplet} \simeq 0.1$ meV as $0.35 \times \Delta_\alpha/\Delta_\beta$ shown in Fig. 3(c) (see SM for details).

We also derived the parameters P and Z_α and plot them as a function of change of g in Fig. 3(c), i.e. $\Delta g = 0$ to 1 between plateaus in Fig. 3(d) and (e), respectively. The pink rectangles, blue triangles, and orange circles represent the parameters derived from the right, center, and left panel of Fig. 3(a), respectively. P indicating the proportion of AR in channel α has the maximum ($\simeq 1$) and Z_α has a minimum at $\Delta g \simeq 0.7$. Our experimental results are obtained by the two-terminal conductance measurement. Therefore the bulk contribution to the channel α becomes maximum at a position displaced from $\Delta g = 0.5$ and likely located between $\Delta g = 0.5$ and 1. Indeed we find that the bulk contribution is maximal at $\Delta g \simeq 0.7$ which is consistent with measurement results on a Hall-bar device (see SM). These results strongly and quantitatively support that channel α is comprised of the spin-resolved QH bulk state and the conductance enhancement originates from the equal-spin AR between the QH bulk state and the superconductor, while the channel β is assigned to normal reflection component in the superconducting bulk gap. We note that the sub-gap feature and the side peaks have been theoretically predicted for the case of spin-singlet and spin-triplet superconducting proximity effect between a topological insulator and a spin-singlet superconductor with magnetic field [38]. There are a few theoretical works describing AR in the QH edge state [10, 39–41], but none focus on the QH state in the plateau-transition regime, and so further theoretical effort is necessary to reproduce the junction properties between superconductor and spin-resolved QH bulk state. From the topological aspects, theory predicts that the chiral topological superconductor state can be realized in superconductor-QH state junctions and therefore such junctions can be utilized to study non-Abelian statistics of the Majorana Fermions localized at the center of vortexes near the plateau-transition regime [21]. Our results indicate that it is possible to induce the proximity gap even in the spin-resolved QH state via equal-spin AR and so realize such chiral topological superconductivity.

In summary, we studied the transport properties of junctions between a NbTi superconductor and an InAs QW in the spin-resolved QH regime. We observed sub-gap features indicating Andreev transport arising from two channels. One equal spin Andreev reflection channel which produces peaks at zero bias, and a conventional Andreev reflection channel producing side peaks. These results indicate that junctions of NbTi and the InAs QW are a promising candidate to experimentally study the spin-triplet superconducting proximity effect in semiconductors and also topological superconductivity.

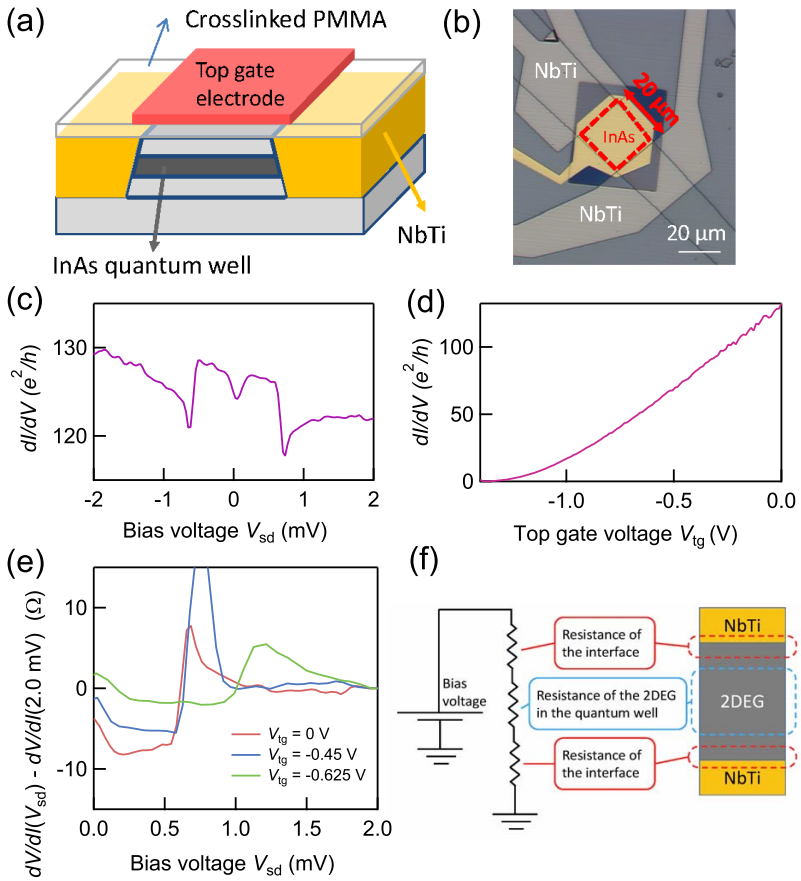

FIG. 1. (a)Cross section of the fabricated device. The edges of the InAs QW are contacted with sputtered NbTi. (b)Optical image of the device. The region surrounded by the red dash line represents the mesa. (c)dI/dV vs. $V_{\rm sd}$ at $V_{\rm tg} = 0$ V and $B = 0$ T. dI/dV measured in the range -0.71 mV $< V_{\rm sd} < 0.71$ mV is enhanced due to AR. (d)dI/dV vs. $V_{\rm tg}$ at $V_{\rm sd} = 0$ V is shown. The InAs QW is completely depleted by $V_{\rm tg}$. (e)dV/dI with dV/dI measured at $V_{\rm sd} = 2.0$ mV subtracted as a function of $V_{\rm sd}$ is shown. The red, blue, and green lines are measured at $V_{\rm tg}$ =0, -0.45, and -0.625 V, respectively. The resistance reduction due to AR decreases as $V_{\rm tg}$ decreases, indicating that $V_{\rm tg}$ tunes the carrier density of not only the center region of the 2DEG but also region near the junctions. (f)Schematic image of an equivalent circuit to our junction devices. The applied $V_{\rm sd}$ is divided between the two junctions and the 2DEG.

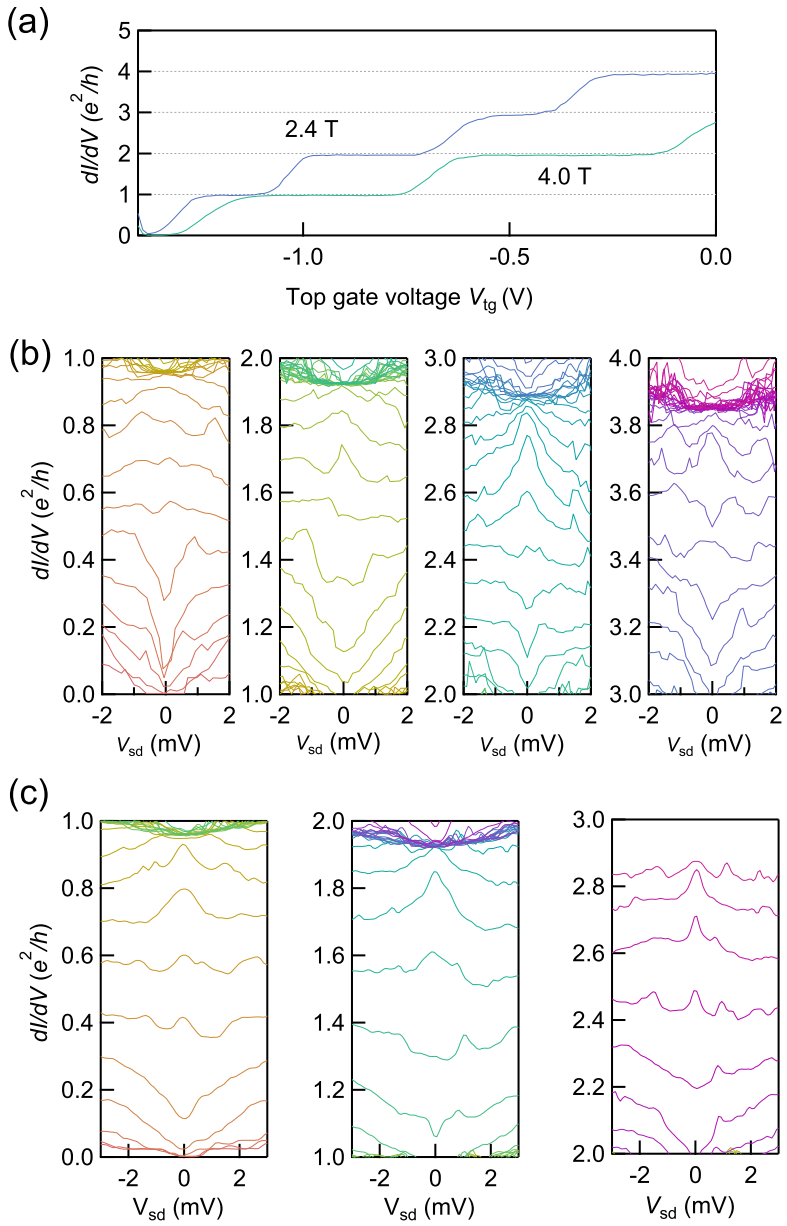

FIG. 2. (a)dI/dV vs. $V_{\rm tg}$ at 2.4 T and 4.0 T with $V_{\rm sd}$ = 0 V. The conductance plateaus are clearly observed on 1, 2, 3, and $4\times e^2/h$. This indicates the Zeeman energy at 2.4 T is enough to resolve the spin degeneracy. (b)Measured dI/dV vs. $V_{\rm sd}$ at 2.4 T for -1.5 V< $V_{\rm tg}$ < 0 V, divided into four panels to clarify the $V_{\rm sd}$ dependence in each plateau-transition regime. dI/dV has a dip structure around $V_{\rm sd}$ = 0 V for $ne^2/h < dI/dV < ne^2/h + 0.5$. In contrast dI/dV has a peak structure for $ne^2/h + 0.5 < dI/dV < ne^2/h + 0.8$. (c)Measured dI/dV vs. $V_{\rm sd}$ at 4.0 T for -1.5 V< $V_{\rm tg}$ < 0 V divided into three panels. The features are similar to those observed in the results obtained at 2.4 T.

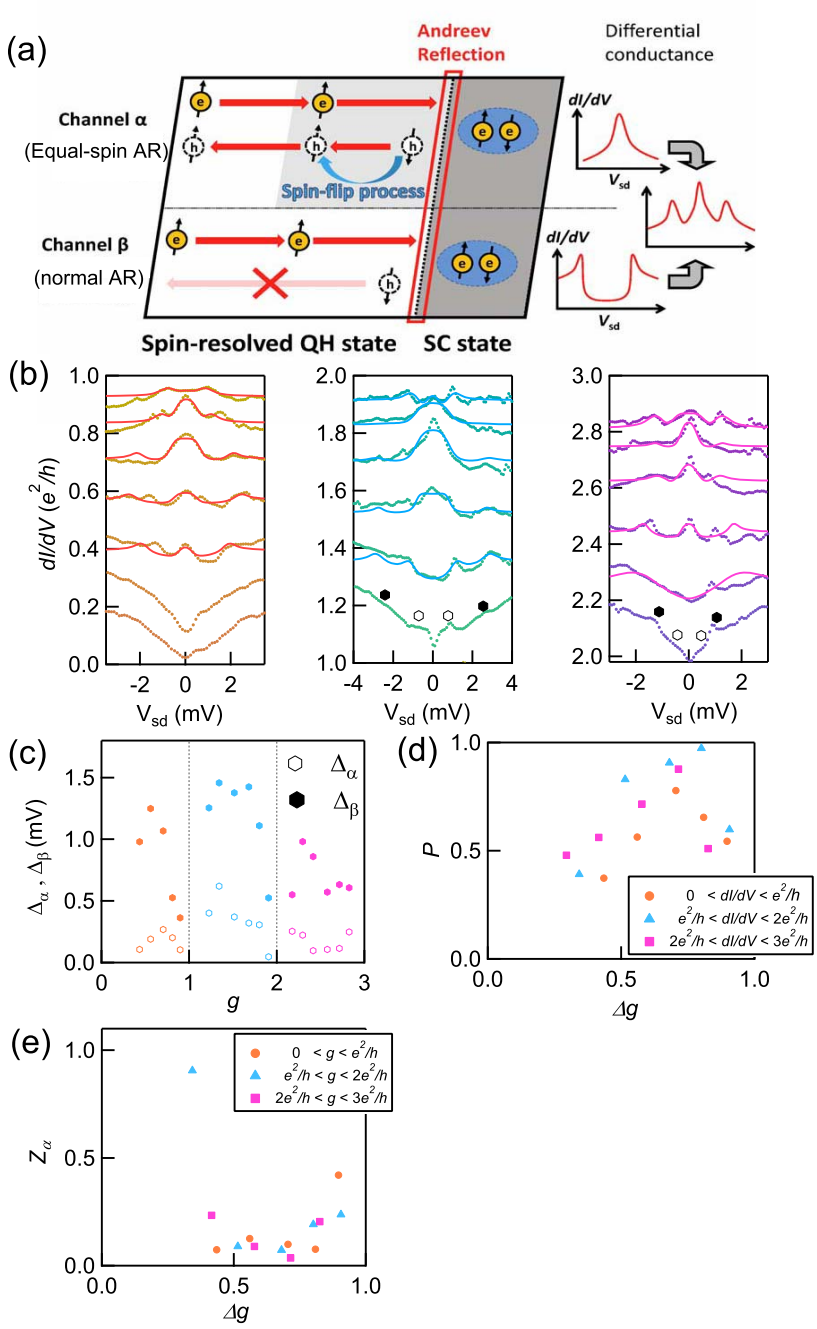

FIG. 3. (a)Schematic of AR in the channel α and β. AR in channel α is intermediated by the spin-flip process, while the reflection in the channel β is not. (b)Measured dI/dV vs. $V_{\rm sd}$ at 4.0 T indicated with dots with fitting results shown as solid lines. The open and closed hexagons are the position of Δ_α and Δ_β without the numerical fitting. (c)Obtained Δ_α and Δ_β are shown as open and closed hexagons, respectively. Δ_β has a convex upward trend in the respective plateau-transition regime. (d)P, indicating the relative contribution of the two channels, is shown as a function of Δg. The orange circles, blue triangles and purple squares are P calculated from the analysis of the left, center, and right panels. (e)Z_α is shown as a function of Δg. The position where Z_α has the minimum is the same as the P.

ACKNOWLEDGMENT

We greatly thank Y. Tanaka, P. Burset, and R. S. Deacon for fruitful discussions. This work was partially supported by Grant-in-Aid for Young Scientific Research (A) (No. JP15H05407), Grant-in-Aid for Scientific Research (A) (No. JP16H02204), Grant-in-Aid for Scientific Research (S) (No. JP26220710), JSPS Research Fellowship for Young Scientists (No. JP14J10600), JSPS Program for Leading Graduate Schools (MERIT) from JSPS, Grant-in-Aid for Scientific Research on Innovative Area, "Nano Spin Conversion Science" (No.JP15H01012), Grant-in-Aid for Scientific Research on Innovative Area, "Topological Materials Science" (Grant No. JP16H00984) from MEXT, CREST, and the Murata Science Foundation.

SUPPLEMENTAL MATERIAL

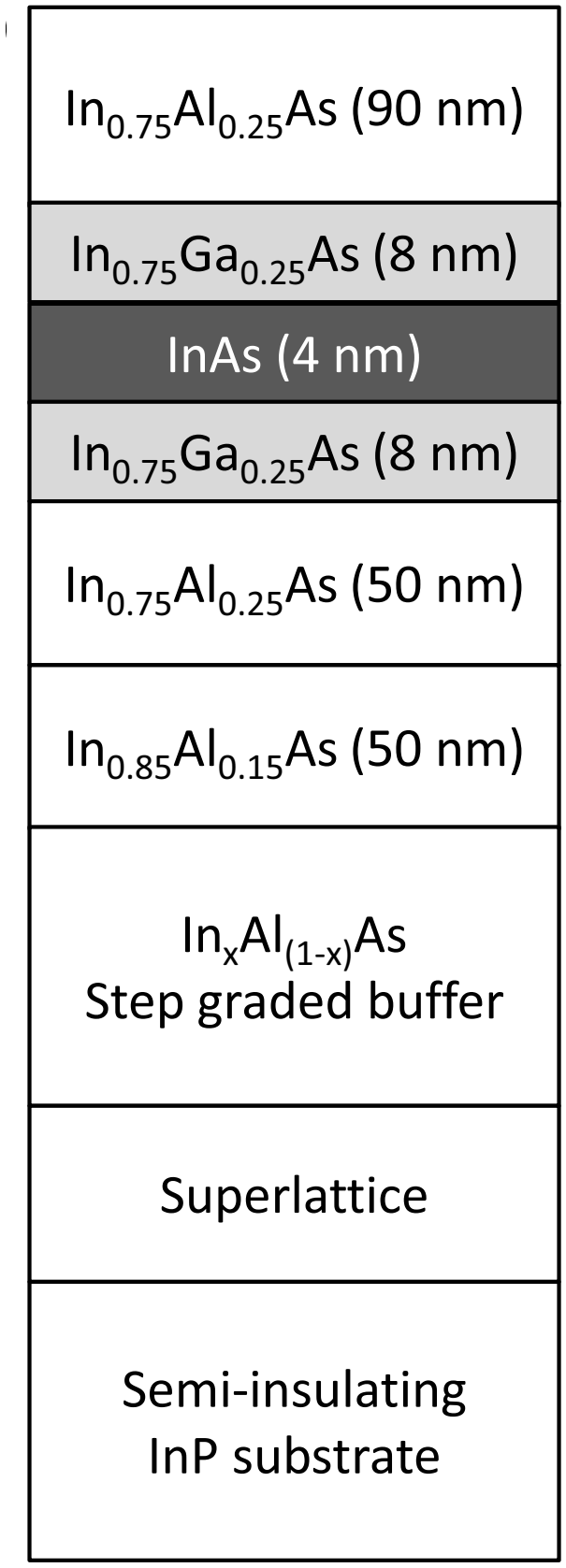

FIG. 4. Schematics of the InAs heterostructure material stack. The2DEG exists in the 4 nm-thick InAs QW.

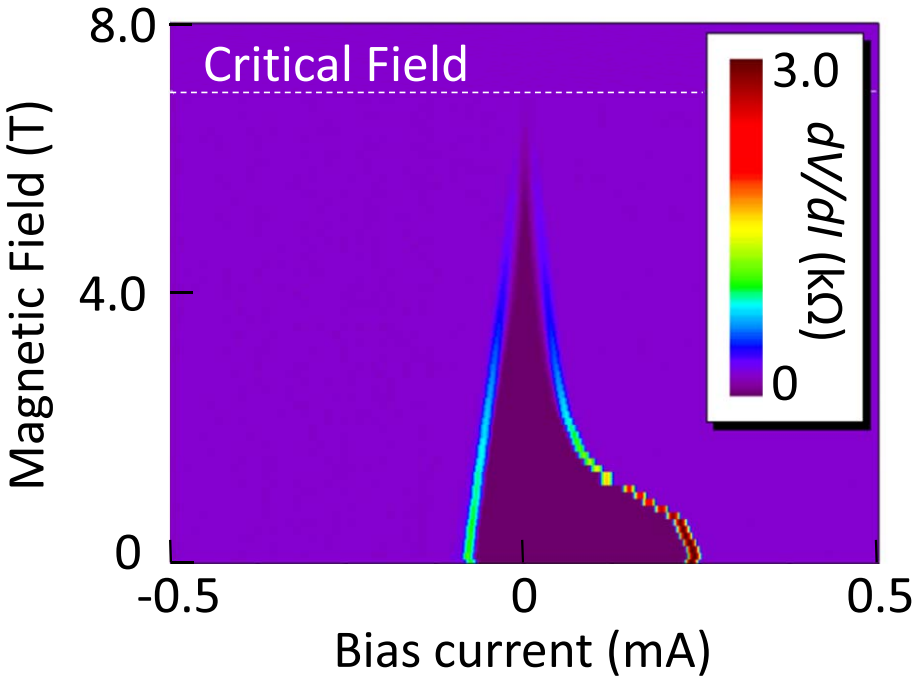

FIG. 5. Measurements of the critical field of a superconducting NbTi 150nm thin film. dV/dI as functions of magnetic field and bias current measured at 2.0 K. The NbTi holds superconductivity when dV/dI is equal to 0. The critical field is 7.0 T.

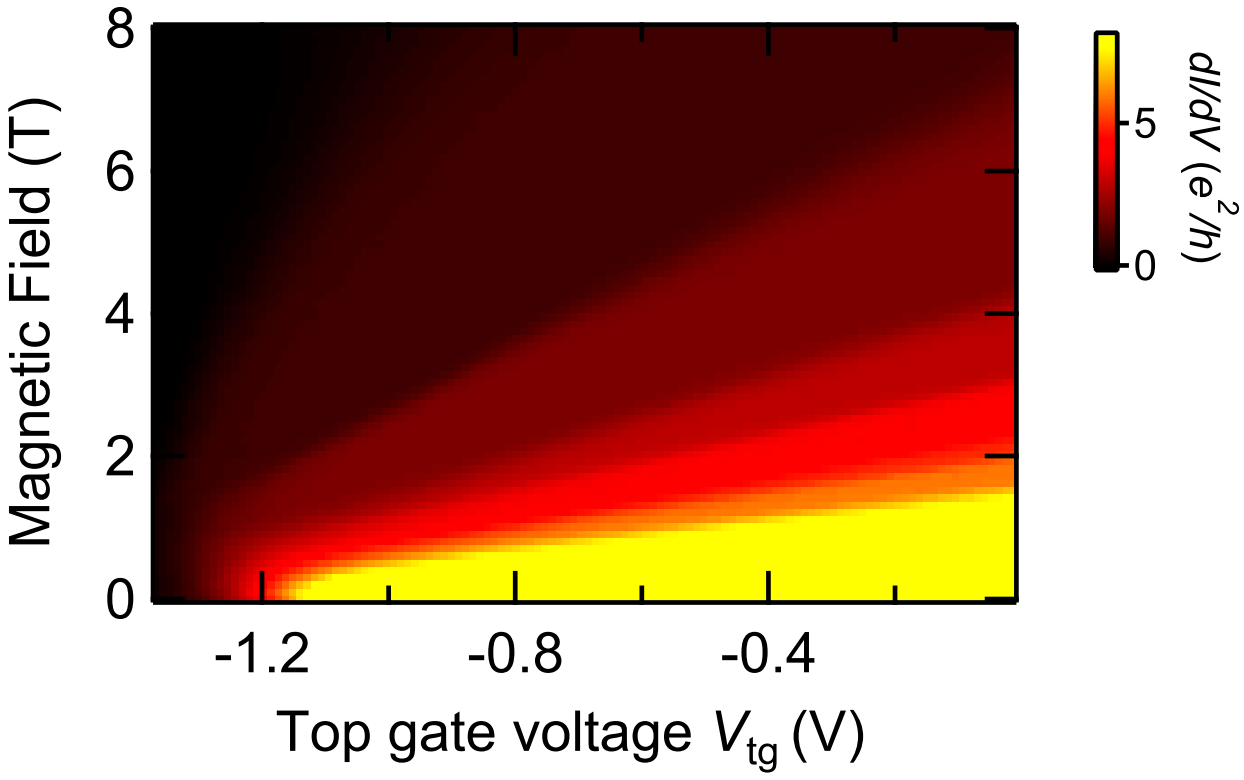

FIG. 6. Conductance as functions of magnetic field and top gate voltage.

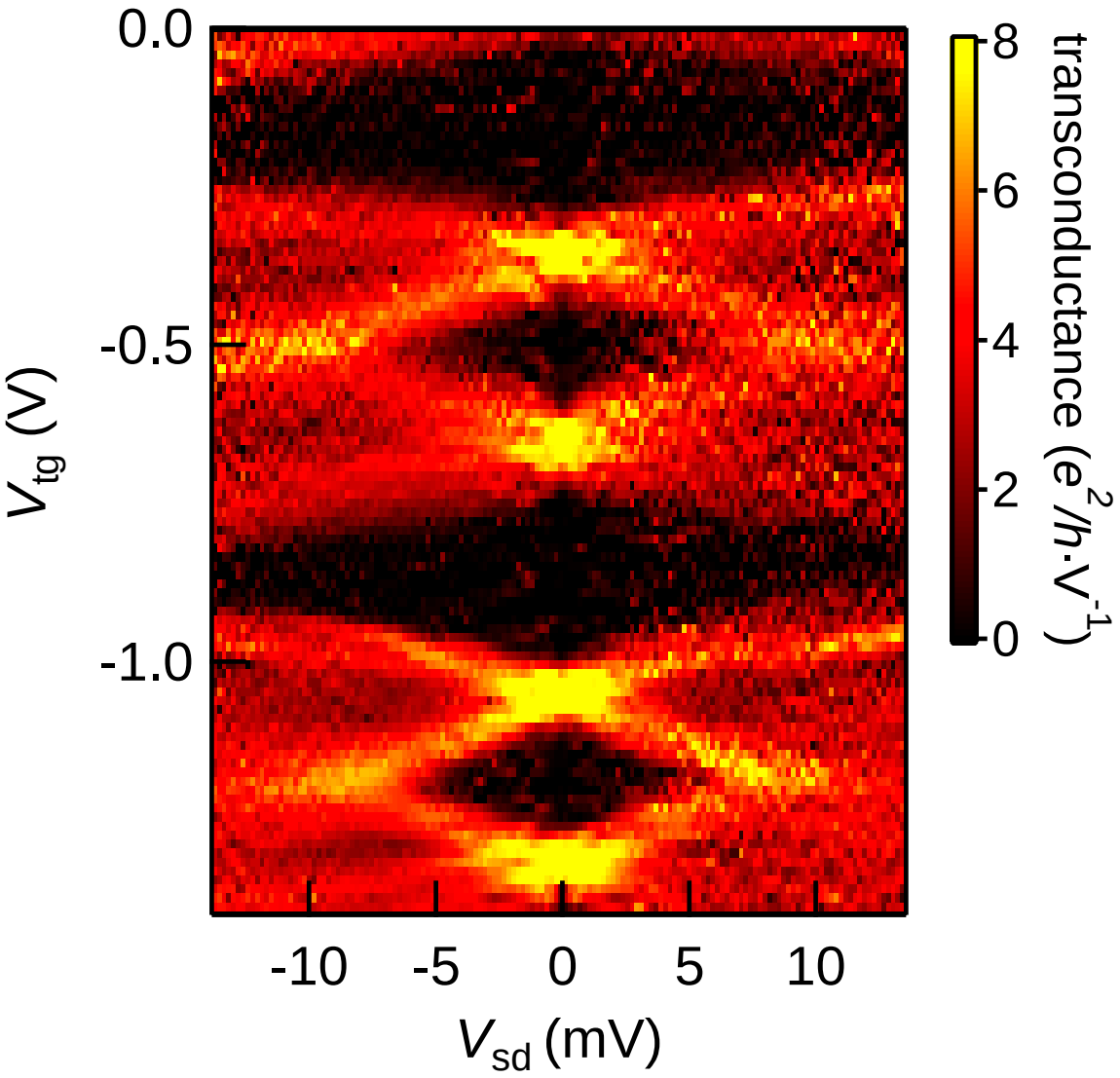

FIG. 7. Transconductance as functions of bias voltage and top gate voltage obtained at 2.4 T.

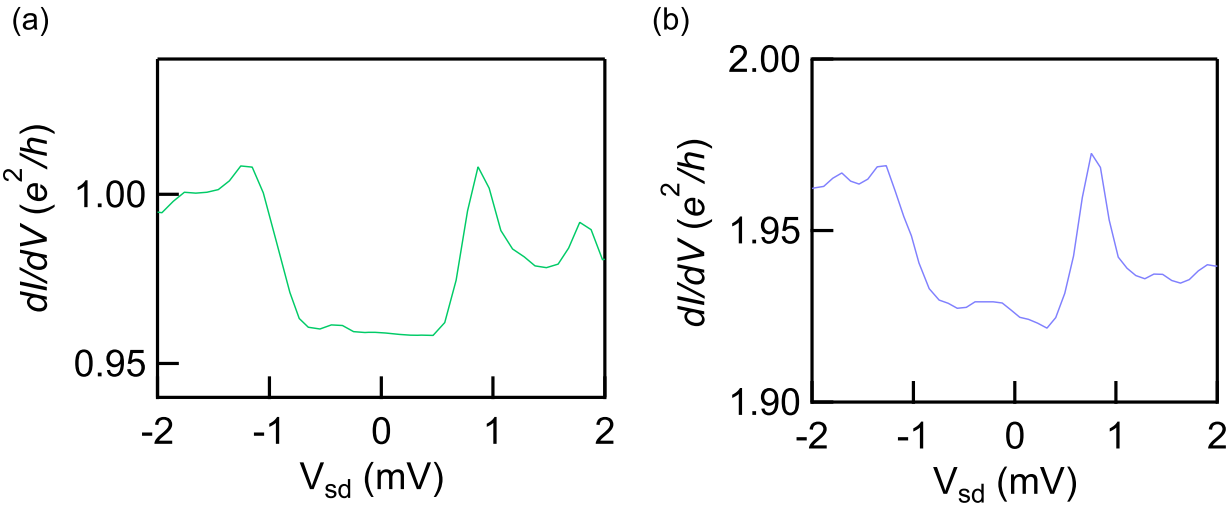

FIG. 8. Typical results of the dI/dV vs $V_{\rm sd}$ in the plateau regime obtained at 4 T are shown. The result on the $\nu = 1$ and 2 plateau is shown in (a) and (b), respectively.

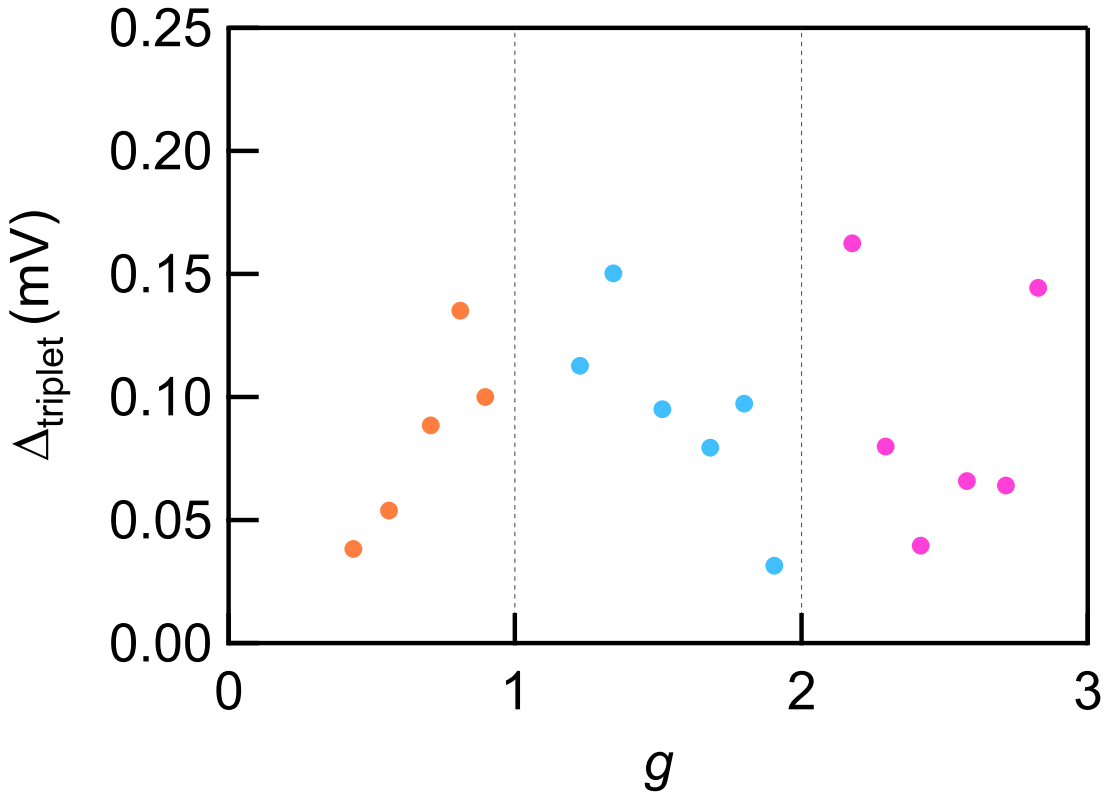

FIG. 9. The calculated spin-triplet superconducting proximity gap energy is shown. The values are ∼0.1 meV.

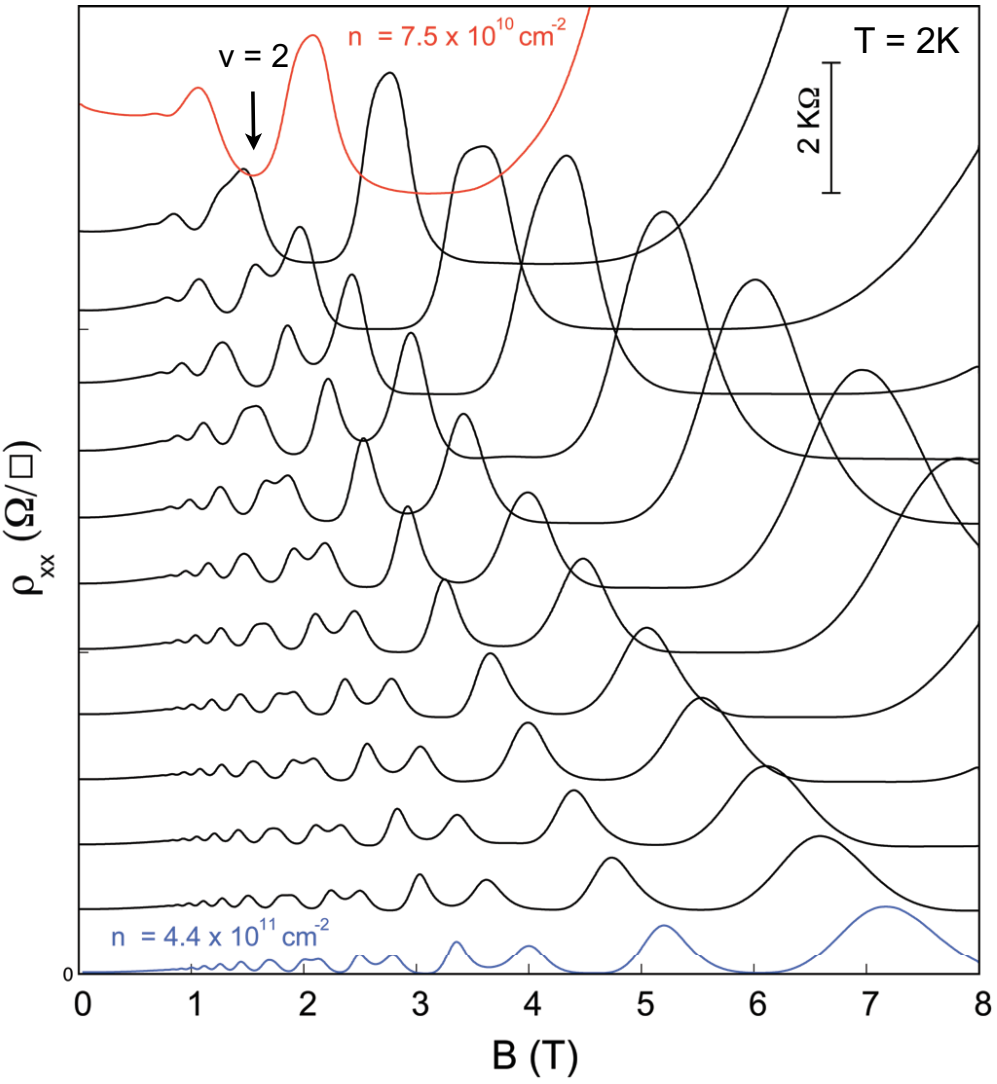

FIG. 10. The sheet resistance as a function of magnetic field is shown. The lines are incrementally shifted for clarity. We measured the resistance in the various carrier density by tuning the gate voltage. We subtract the peak height of the resistance around 4 T.

Device fabrication

We used an InAs QW grown by molecular beam epitaxy with the density 3×10^{11} cm^{-2} and the mobility 3×10^5 cm^{2}V^{-1}s^{-1}. The 2DEG is formed in the 4 nm-thick InAs layer. The material stack of the InAs heterostructure is schematically shown in Fig. 4. A mesa was first defined in the substrate by wet etching with an etchant based on H_3PO_4. Then, NbTi was sputtered to form the superconducting electrodes on the mesa edges, following a procedure of wet etching to make the clean edge exposed, sulfur passivation to avoid oxidization of the edge, and in-situ Ar plasma cleaning. Finally a gate electrode metal of Titanium and Gold was deposited on top to address the low QH filling regime even under a low magnetic field. The top gate is placed on an insulating layer made from cross-linked PMMA. This fabrication procedure creates no superconducting material on the top surface of the mesa. This is specially devised to control the carrier density not only of the mesa but also near the junction using the top gate voltage (discussed later). The two junctions are separated by 20 μm, so this device is assumed to have two independent contact regions.

NbTi superconductivity

To characterize the superconducting properties of the NbTi, we performed a current-bias measurement of the differential resistance dV/dI at various out-of-plane magnetic fields B for a 150 nm-thick NbTi thin film device at 2 K which is lower than the NbTi critical temperature of 6.5 K. The measured data shows a supercurrent branch as dV/dI=0 kΩ in dark purple near the zero current bias in Fig. 5. From this data, we evaluate the critical field of B =7.0 T. Herein, the coexistence of superconducting state and QH states can be realized if the 2DEG is in the spin-resolved QH regime for $B < 7.0$ T.

Superconducting proximity at 0 T

In Fig. 2(a) and (c) in the main text, there are dip structures around $V_{\rm sd} = \pm 0.7$ mV. These dip structures cannot be expected from the normal BTK model. These dip structures have also been reported in experimental studies of junctions of three dimensional topological insulators and superconductor [42]. Some theoretical works predict existence of spin-triplet superconducting proximity on such junctions which generate the dip structures [37, 38]. In our case, strong spin-orbit interaction on the interface can affect the superconducting proximity even at 0 T and invokes finite spin-flip process. Therefore, we suspect that the dip structure may be related to the spin-triplet superconducting proximity even at 0 T.

Transconductance in the QH regime

We measured the conductance as functions of magnetic field and top gate voltage in order to estimate quality of our InAs quantum Hall effect and Zeeman effect. Figure 6 shows the conductance as functions of B and $V_{\rm tg}$. As seen in this figure, clear quantized conductance plateaus appear at $B > 0.6$ T and the Zeeman splitting is found at $B >\sim 1$ T. 2.4 and 4 T is large enough to study the coexistence between the spin-resolved QH state and superconductor. Furthermore, we measured the transconductance defined by the deviation of dI/dV at 2.4 T. The results are plotted in Fig. 7. The diamond-shaped structure can be found. We focus on the bright areas, namely the plateau-transition regime in the main text.

Sub-gap feature in QH plateau regime

In the main text, we focus on the sub-gap feature in QH plateau-transition regime. In this section, we show the measured dI/dV vs $V_{\rm sd}$ in the plateau regime. The typical results obtained at 4 T are shown in Fig. 8. Panel (a) and (b) indicates the result on the $\nu = 1$ and 2 plateau, respectively. Even in the plateau regime, there is a sub-gap feature with a small dip or gap-like structure. These results are similar to the sub-gap features observed for $\Delta g < 0.4$ of Fig. 3(b) and (c) in the main text. The estimated gap from these sub-gap features are nearly equal to the 0.35 mV calculated from the superconducting gap at 0 T. This supports our assumption in the main text that the spin-singlet

superconducting proximity gap at 4 T is the same as the superconducting gap obtained at 0 T. We conclude that the QH edge states don't contribute to the Andreev reflection in the device.

Numerical calculation

We executed the numerical calculation using the model in which we assume the two channels, α and β. The fitting parameters are the superconducting gaps Δ_α and Δ_β, barrier strength Z_α ($Z_\beta = 1$), normal state interface conductance G_n, effective temperature ω, the relative contribution of channel α, P and offset conductance $G_{\rm offset}$. We define $G_{\rm int}^{\alpha\beta}(V_{\rm sd}, Z_\alpha, T, \Delta_\alpha, \Delta_\beta)$ as eqn. (2) in the main text. Then the fitting function can be written as

$$\Big(\frac{1}{G_n \cdot G_{\rm int}^{\alpha\beta}(V_{\rm sd}, Z_\alpha, T, 2\Delta_\alpha, 2\Delta_\beta)} + \frac{1}{G_{\rm offset}}\Big)^{-1}.$$

We take care to confirm that our device has two independent superconducting-QH bulk state junctions. Therefore, the sub-gap features and the position in $V_{\rm sd}$ of the side peaks are consistent with $2\Delta_\alpha$ and $2\Delta_\beta$. To account for the effective temperature, we approximated the deviation of the Fermi-Dirac distribution function in eqn. (1) in the main text as the Gaussian function, $\exp\left(-((E - V_{\rm sd})/2\omega)^2\right)$, where ω is ideally equal to T but now ω includes the broadening due to inelastic scattering, inhomogeneity of the gap and the local heating [43, 44]. To execute the fitting, we constrict the fitting ranges for all the parameters, and especially we tightly constrict the Δ_α and Δ_β from the curve shapes. In order to reproduce the curve shape around the zero bias voltage, we changed the fitting range for each of the curves because the differential conductance of the 2DEG appears as background and the conductance has a large dependence on the bias voltage near the plateau regime. Due to this background dependence, we could not reproduce the curve shapes in the two lower curves of the left panel and middle panel, and the lowest curve of the right panel in Fig.4(b) of the main text. In these cases, we evaluated only Δ_α and Δ_β from the sub-gap peak features ($2\Delta_\alpha$ and $2\Delta_\beta$ are indicated on the panels in Fig.4(b) as open and closed hexagons). Our fitting scheme includes many free parameters and results are sensitive to the constriction of the variable range. However, the estimated gap energies and P produce relatively constant results with different fitting ranges, so we think it is valuable to discuss these parameters. All fits are executed with a genetic algorithm (GenCurvefit package for Igor Pro).

Calculation of the proximity gap energy

As written in the main text, we analyzed our experimental data with the model to evaluate Δ_α and Δ_β, the superconducting gap energies. However, these values are enlarged from the true bulk and proximity superconducting gap energies due to dissipation induced from the bulk state of the mesa. In the plateau regime, the transport is non-dissipative in the mesa, while the transport is dissipative in the plateau-transition regime due to the QH bulk state. Herein, in the plateau-transition regime, applied $V_{\rm sd}$ between two superconductors is divided into the voltage on the junctions and on the mesa, then the deduced Δ_β gives a larger gap energy as the contribution of the QH bulk state in the transport becomes larger. The equivalent circuit is represented in Fig. 2(d) in the main text. Consequently, Δ_β produces a peak in the middle of the plateau-transition regime where the bulk contribution becomes maximum. The true bulk superconducting gap energies (corresponding to the gap for channel β), 0.35 meV, can be evaluated from Δ_β near the plateau regime. From this gap energy, we calculated the true superconducting proximity gap energy, ~ 0.1 meV as $0.35 \times \Delta_\alpha/\Delta_\beta$. The calculated gap, $\Delta_{\rm triplet}$ as a function of g, dI/dV at $V_{\rm sd} = 3.5$ mV in unit of e^2/h is shown in Fig.9.

The maximum position of the bulk contribution

Our results for P and Z_α have a maximum and minimum, respectively, at $\Delta g \sim 0.7$. In this section, we estimate how large ρ_{xx} should be to make the bulk contribution have a maximum at $\Delta g \sim 0.7$.

As the shape of our device is square, the two-terminal conductance is written by $G_{2t} = \sqrt{\sigma_{xx} + \sigma_{xy}}$. σ_{xx} and σ_{xy} are the longitudinal conductivity and Hall conductivity [45–47], respectively. σ_{xx} has a maximum when the bulk contribution is maximum and the situation is given by $\sigma_{xy} = 0.5e^2/h + ne^2/h$ ($n = 0, 1, 2, 3...$), at which change in the filling factor $\Delta\nu$ is equal to 0.5. Herein, if the bulk contribution is maximum at $\Delta g \sim 0.7$ (namely $G_{2t} = 0.7e^2/h + ne^2/h$), $\sigma_{xx}(\sigma_{xy})$ should be $0.49e^2/h$ ($0.5e^2/h$), $0.80e^2/h$ ($1.5e^2/h$), and $1.02e^2/h$ ($2.5e^2/h$) in the $n = 0, 1,$ and 2

cases, respectively. From these conductivity, we can calculate the longitudinal resistance,$\rho_{xx} = \sigma_{xx}/(\sigma_{xx}^2 + \sigma_{xy}^2)$, resulting in $1.0h/e^2$ ($\sim$ 26kΩ), $0.28h/e^2$($\sim$ 7.0kΩ), and $0.14h/e^2$($\sim$ 3.6kΩ) in the $n = 0, 1,$ and 2 cases, respectively. The calculated longitudinal resistance should be obtained when the bulk contribution is maximum, meaning ρ_{xx} is maximum with the calculated resistance in the region corresponding to the plateau-transition regime. We measured a Hall bar device at 2 K, fabricated from the same InAs quantum well wafer as we used for the superconducting devices and the results are shown in Fig. 10. ρ_{xx} has some peaks consistent with the finite bulk contribution. The maximum of ρ_{xx} at 4 T is at 4 kΩ and 1.5 kΩ corresponding to the $n =$ 1and 2 cases, respectively. The measured resistances are comparable to the estimated resistance based on the assumption that the bulk contribution is maximum at $\Delta g \sim 0.7$ ($G_{2t} = 0.7e^2/h + ne^2/h$).

* matsuo@ap.t.u-tokyo.ac.jp

[1] A. F. Andreev, Sov. Phys. JETP. **19**, 1228 (1964).
[2] F. S. Bergeret, A. F. Volkov, and K. B. Efetov, Rev. Mod. Phys. **77**, 1321 (2005).
[3] R. S. Keizer, S. T. B. Goennenwein, T. M. Klapwijk, G. Miao, G. Xiao, and A. Gupta, Nature **439**, 825 (2010).
[4] Y. Asano, Y. Tanaka, and A. A. Golubov, Phys. Rev. Lett. **98**, 107002 (2007).
[5] Y. Asano, Y. Sawa, Y. Tanaka, and A. A. Golubov, Phys. Rev. B **76**, 224525 (2007).
[6] J. W. A. Robinson, J. D. S. Witt, and M. G. Blamire, Science **329**, 59 (2010).
[7] C. Visani, Z. Sefrioui, J. Tornos, C. Leon, J. Briatico, M. Bibes, A. Barthelemy, J. Santamaria, and J. E. Villegas, Nature Physics **8**, 539 (2012).
[8] J. Linder and J. W. A. Robinson, Nature Physics **11**, 307 (2015).
[9] M. Eschrig and T. Lofwander, Nature Physics **4**, 138 (2008).
[10] J. A. M. van Ostaay, A. R. Akhmerov, and C. W. J. Beenakker, Phys. Rev. B **83**, 195441 (2011).
[11] J. Luo, H. Munekata, F. F. Fang, and P. J. Stiles, Phys. Rev. B **38**, 10142 (1988).
[12] E. A. de Andrada e Silva, G. C. La Rocca, and F. Bassani, Phys. Rev. B **55**, 16293 (1997).
[13] J. Nitta, T. Akazaki, H. Takayanagi, and T. Enoki, Phys. Rev. Lett. **78**, 1335 (1997).
[14] J. P. Heida, B. J. van Wees, J. J. Kuipers, T. M. Klapwijk, and G. Borghs, Phys. Rev. B **57**, 11911 (1998).
[15] H. Takayanagi and T. Akazaki, Physica B: Condensed Matter **249-251**, 462 (1998).
[16] J. Eroms, D. Weiss, J. D. Boeck, G. Borghs, and U. Zülicke, Phys. Rev. Lett. **95**, 107001 (2005).
[17] P. Rickhaus, M. Weiss, L. Marot, and C. Schonenberger, Nano Letters **12**, 1942 (2012), pMID: 22417183.
[18] K. Komatsu, C. Li, S. Autier-Laurent, H. Bouchiat, and S. Guéron, Phys. Rev. B **86**, 115412 (2012).
[19] Z. Wan, A. Kazakov, M. J. Manfra, L. N. Pfeiffer, K. W. West, and L. P. Rokhinson, Nature Communications **6**, 7426 (2015).
[20] F. Amet, C. T. Ke, I. V. Borzenets, J. Wang, K. Watanabe, T. Taniguchi, R. S. Deacon, M. Yamamoto, Y. Bomze, S. Tarucha, and G. Finkelstein, Science **352**, 966 (2016).
[21] X.-L. Qi, T. L. Hughes, and S.-C. Zhang, Phys. Rev. B **82**, 184516 (2010).
[22] L. Fu and C. L. Kane, Phys. Rev. Lett. **100**, 096407 (2008).
[23] M. Z. Hasan and C. L. Kane, Rev. Mod. Phys. **82**, 3045 (2010).
[24] V. Mourik, K. Zuo, S. M. Frolov, S. R. Plissard, E. P. A. M. Bakkers, and L. P. Kouwenhoven, Science **336**, 1003 (2012).
[25] A. Das, Y. Ronen, Y. Most, Y. Oreg, M. Heiblum, and H. Shtrikman, Nature Physics **8**, 887 (2012).
[26] L. P. Rokhinson, X. Liu, and J. K. Furdyna, Nature Physics **8**, 795 (2012).
[27] S. Nadj-Perge, I. K. Drozdov, J. Li, H. Chen, S. Jeon, J. Seo, A. H. MacDonald, B. A. Bernevig, and A. Yazdani, Science **346**, 602 (2014).
[28] E. Bocquillon, R. S. Deacon, J. Wiedenmann, P. Leubner, T. M. Klapwijk, C. Brune, K. Ishibashi, H. Buhmann, and L. W. Molenkamp, Nature Nanotechnology **12**, 137 (2016).
[29] J. Wiedenmann, E. Bocquillon, R. S. Deacon, S. Hartinger, O. Herrmann, T. M. Klapwijk, L. Maier, C. Ames, C. Brune, C. Gould, A. Oiwa, K. Ishibashi, S. Tarucha, H. Buhmann, and L. W. Molenkamp, Nature Communications **7**, 10303 (2016).
[30] S. M. Albrecht, A. P. Higginbotham, M. Madsen, F. Kuemmeth, T. S. Jespersen, J. Nygard, P. Krogstrup, and C. M. Marcus, Nature **531**, 206 (2016).
[31] R. S. Deacon, J. Wiedenmann, E. Bocquillon, F. Dominguez, T. M. Klapwijk, P. Leubner, C. Brune, E. M. Hankiewicz, S. Tarucha, K. Ishibashi, H. Buhmann, and L. W. Molenkamp, arXiv , 1603.09611 (2016).
[32] J. Shabani, S. Das Sarma, and C. J. Palmstrøm, Phys. Rev. B **90**, 161303 (2014).
[33] J. Shabani, A. P. McFadden, B. Shojaei, and C. J. Palmstrøm, Applied Physics Letters **105**, 262105 (2014).
[34] G. E. Blonder, M. Tinkham, and T. M. Klapwijk, Phys. Rev. B **25**, 4515 (1982).
[35] H. Irie, C. Todt, N. Kumada, Y. Harada, H. Sugiyama, T. Akazaki, and K. Muraki, Phys. Rev. B **94**, 155305 (2016).
[36] H. X. Tang, Z. D. Wang, and Y. Zhang, Z. Phys. B **101**, 359 (1996).
[37] P. Burset, F. Keidel, Y. Tanaka, N. Nagaosa, and B. Trauzettel, Phys. Rev. B **90**, 085438 (2014).
[38] P. Burset, B. Lu, G. Tkachov, Y. Tanaka, E. M. Hankiewicz, and B. Trauzettel, Phys. Rev. B **92**, 205424 (2015).
[39] H. Hoppe, U. Zülicke, and G. Schön, Phys. Rev. Lett. **84**, 1804 (2000).

[40] F. Giazotto, M. Governale, U. Zülicke, and F. Beltram, Phys. Rev. B **72**, 054518 (2005).
[41] I. M. Khaymovich, N. M. Chtchelkatchev, I. A. Shereshevskii, and A. S. Mel'nikov, EPL (Europhysics Letters) **91**, 17005 (2010).
[42] M. Snelder, M. P. Stehno, A. A. Golubov, C. G. Molenaar, T. Scholten, D. Wu, Y. K. Huang, W. G. van der Wiel, M. S. Golden, and A. Brinkman, arXiv **1506**, 05923 (2015).
[43] G. T. Woods, R. J. Soulen, I. Mazin, B. Nadgorny, M. S. Osofsky, J. Sanders, H. Srikanth, W. F. Egelhoff, and R. Datla, Phys. Rev. B **70**, 054416 (2004).
[44] J. P. DeGrave, A. L. Schmitt, R. S. Selinsky, J. M. Higgins, D. J. Keavney, and S. Jin, Nano Letters **11**, 4431 (2011), pMID: 21923114, http://dx.doi.org/10.1021/nl2026426.
[45] H. J. Lippmann and R. Kuhrt, Z. Naturforsch. A **13**, 462 (1958).
[46] H. H. Jensen and H. Smith, Journal of Physics C: Solid State Physics **5**, 2867 (1972).
[47] D. A. Abanin and L. S. Levitov, Phys. Rev. B **78**, 035416 (2008).